AGU PUBLICATIONS

JGR

Journal of Geophysical Research: Atmospheres

RESEARCH ARTICLE
10.1002/2017JD027187

Key Points:
- Satellite data of clouds and aerosols are used to investigate the aerosol indirect effect from a climatology perspective
- Sensitive regimes and active regions of aerosol indirect effects have been identified in long-term averages over the global oceans
- Our results based on the satellite observation are valuable for the evaluation and improvement of the global climate models

Correspondence to:
X. Zhao,
xuepeng.zhao@noaa.gov

Citation:
Zhao, X., Liu, Y., Yu, F., & Heidinger, A. K. (2018). Using long-term satellite observations to identify sensitive regimes and active regions of aerosol indirect effects for liquid clouds over global oceans. *Journal of Geophysical Research: Atmospheres*, *123*, 457–472. https://doi.org/10.1002/2017JD027187

Received 23 MAY 2017
Accepted 13 NOV 2017
Accepted article online 16 NOV 2017
Published online 10 JAN 2018

Published 2017. This article is a US Government work and is in the public domain in the USA.
This is an open access article under the terms of the Creative Commons Attribution-NonCommercial-NoDerivs License, which permits use and distribution in any medium, provided the original work is properly cited, the use is non-commercial and no modifications or adaptations are made.

Using Long-Term Satellite Observations to Identify Sensitive Regimes and Active Regions of Aerosol Indirect Effects for Liquid Clouds Over Global Oceans

Xuepeng Zhao[1], Yangang Liu[2], Fangquan Yu[3], and Andrew K. Heidinger[4]

[1]National Centers for Environmental Information, NOAA/NESDIS, Silver Spring, MD, USA, [2]Environmental and Climate Sciences Department, Brookhaven National Laboratory, Upton, NY, USA, [3]Atmospheric Sciences Research Center, State University of New York at Albany, Albany, NY, USA, [4]Center for Satellite Applications and Research, NOAA/NESDIS, Madison, WI, USA

Abstract Long-term (1981–2011) satellite climate data records of clouds and aerosols are used to investigate the aerosol-cloud interaction of marine water cloud from a climatology perspective. Our focus is on identifying the regimes and regions where the aerosol indirect effects (AIEs) are evident in long-term averages over the global oceans through analyzing the correlation features between aerosol loading and the key cloud variables including cloud droplet effective radius (CDER), cloud optical depth (COD), cloud water path (CWP), cloud top height (CTH), and cloud top temperature (CTT). An aerosol optical thickness (AOT) range of $0.13 < \mathrm{AOT} < 0.3$ is identified as the sensitive regime of the conventional first AIE where CDER is more susceptible to AOT than the other cloud variables. The first AIE that manifests as the change of long-term averaged CDER appears only in limited oceanic regions. The signature of aerosol invigoration of water clouds as revealed by the increase of cloud cover fraction (CCF) and CTH with increasing AOT at the middle/high latitudes of both hemispheres is identified for a pristine atmosphere ($\mathrm{AOT} < 0.08$). Aerosol invigoration signature is also revealed by the concurrent increase of CDER, COD, and CWP with increasing AOT for a polluted marine atmosphere ($\mathrm{AOT} > 0.3$) in the tropical convergence zones. The regions where the second AIE is likely to manifest in the CCF change are limited to several oceanic areas with high CCF of the warm water clouds near the western coasts of continents. The second AIE signature as represented by the reduction of the precipitation efficiency with increasing AOT is more likely to be observed in the AOT regime of $0.08 < \mathrm{AOT} < 0.4$. The corresponding AIE active regions manifested themselves as the decline of the precipitation efficiency are mainly limited to the oceanic areas downwind of continental aerosols. The sensitive regime of the conventional AIE identified in this observational study is likely associated with the transitional regime from the aerosol-limited regime to the updraft-limited regime identified for aerosol-cloud interaction in cloud model simulations.

Plain Language Summary Long-term satellite observations of cloud and aerosol have been used to investigate the aerosol effect on marine water cloud from the perspective of climatology. Identifying the regimes and regions where the aerosol effect may manifest clearly in a sense of long-term average over the global oceans is the focus of this study. Several sensitive regimes of aerosol loading and active regions of aerosol effect on the cloud have been identified for the first time in long-term averages of cloud and aerosol variables over the global oceans. The results of this study based on the long-term averaged satellite observation are valuable for the evaluation and improvement of the aerosol effect on cloud in global climate models, which are only evaluated and assessed so far against instantaneous or short-term averaged observations.

1. Introduction

Atmospheric aerosols alter cloud properties and lifetime (Albrecht, 1989; Breon et al., 2002; Twomey, 1977; Twomey et al., 1984), which may further impact the radiation budget and precipitation efficiency (Coakley et al., 1987; Rosenfeld et al., 2008) and eventually modify the energy and hydrological cycles of the Earth climate system (Charlson et al., 1992; Ramanathan et al., 2001). The aerosol-induced modification of microphysical and hence radiative properties, amount, and lifetime of clouds is generally named as the aerosol indirect effect (AIE). Due to the short lifetime, inhomogeneous spatial distribution, and complex chemical compositions and size distributions of aerosols, it is difficult to quantify the aerosol effect on climate,

especially in view of additional factors, such as cloud dynamics and thermal dynamics, affecting clouds and precipitation. This results in large uncertainties in the determination of anthropogenic global warming associated with increasing greenhouse gases, since aerosols mainly exert a cooling effect that counteracts the warming effect of greenhouse gases (IPCC, 2014).

The large uncertainties and considerable controversies in the AIE may be due to the buffering effect of aerosol-cloud-precipitation system as indicated by Stevens and Feingold (2009). They pointed out that the AIE processes in such buffered systems entangle with other processes (e.g., cloud dynamics) so that it is very difficult to clearly separate them and to quantify their effect accordingly with existing tools and methodologies. They further pointed out whether an AIE process that will be manifested in the buffered system is regime dependent so that future research should aim at understanding the aerosol, cloud, and precipitation regimes with the clearest AIE signatures. Such regime-related studies have been pursued actively by using numerical model simulations (e.g., Chen et al., 2016; Reutter et al., 2009) and regional instantaneous or short-term observations (e.g., Kaufman et al., 2005; Koren et al., 2014; Yuan et al., 2008).

In this paper, we present a study on the sensitive regimes and active regions of the AIE for marine water clouds over the global oceans from a perspective of large-scale long-term average (also called large-scale climatology). To identify robust AIE signatures or imprints in large spatial scales for temporally averaged state of aerosol-cloud-precipitation system, global long-term averaged aerosol and cloud satellite observations are used in our analysis, which are described in section 2 along with the analysis methodology; aerosol optical thickness (AOT) regimes in which the corresponding AIEs are sensitive are identified and discussed in section 3; the regions where the AIE signatures are the clearest over the global oceans are presented in sections 4; summary and conclusions are given in the closing section.

2. Satellite Data and Analysis Methodology

This study uses Version 3 of the Advanced Very High Resolution Radiometer (AVHRR) AOT climate data record (CDR) (Zhao et al., 2016) from the National Oceanic and Atmospheric Administration (NOAA) operational satellites and Version 5.3 of NOAA Pathfinder Atmospheres-Extended (PATMOS-x) AVHRR cloud CDR products (Heidinger et al., 2014).

PATMOS-x cloud CDR products are in $0.1° \times 0.1°$ equal angle orbital grid and named as the Level-2b products, which are retrieved using the intercalibrated AVHRR global area coverage (GAC) radiance data (see Heidinger et al., 2014; Walther & Heidinger, 2012). The intercalibrated AVHRR GAC radiance is also cross calibrated with more advanced Moderate Resolution Imaging Spectroradiometer (MODIS) radiance (Cao et al., 2004, 2008; Heidinger et al., 2002, 2010). Cloud variables used in the analyses are cloud droplet effective radius (CDER), cloud optical depth (COD), cloud water path (CWP), cloud cover fraction (CCF), cloud top height (CTH), and cloud top temperature (CTT) for marine liquid clouds, including both warm and supercooled water clouds without ice formed (see Pavolonis et al., 2005). They are output together with the intercalibrated and cross-calibrated AVHRR radiances and selected ancillary data (e.g., surface types) as the Level-2b daily CDR products, which allow other CDRs to be generated from the PATMOS-x CDR data for further applications. PATMOS-x CDR data span from 1978 to present and should extend to at least 2020. Only the data after 1980 are used in this study in view of many missing observations in the first 3 years (1978–1980) of AVHRR data records.

AVHRR AOT CDR is derived over global water (or ocean) surface for the 0.63 μm channel using a two-channel AVHRR aerosol retrieval algorithm (Zhao et al., 2004) from AVHRR clear-sky reflectance in daytime, which is determined from the PATMOS-x AVHRR all-sky reflectance and cloud probability products contained in Version 5.3 PATMOS-x AVHRR reflectance/cloud CDRs (Heidinger et al., 2014). The data period spans from 1981 to 2011, and the spatial resolution is $0.1° \times 0.1°$ on the equal angle grid. AVHRR AOT retrieval can be problematic at large solar zenith angles (Ignatov & Stowe, 2002; Stowe et al., 1997) beyond 60°N and 60°S latitudes (especially for the winter months), which may result in poor data sampling in monthly AOT averages in these latitudinal regions. At the same time, cloud detection is degraded over bright snow and ice surfaces at polar latitudes. Thus, we confine our analysis to within 60°S and 60°N over the global oceans. Thirty-one years (1981–2011) of monthly averaged products of AVHRR AOT CDR and PATMOS-x AVHRR cloud CDRs are used in this study. Specifically, the monthly mean products of AOT and the cloud variables of each year are obtained by averaging all daily observational records in a month. The 31 years monthly mean records (total 372 months) are further averaged to obtain long-term averaged monthly mean products for our analysis in the following sections.

To facilitate the analyses and discussions below, some concepts and items related to the aerosol-cloud interaction are first summarized and defined here. Aerosol-cloud interaction generally includes aerosol indirect effect (or negative effect) and aerosol invigoration effect (positive effect). Conventionally, the aerosol indirect effect is further divided into two main types. The first type is called the first aerosol indirect effect (also named "albedo effect" or "Twomey effect"), which refers to the microphysically induced effect by aerosols as cloud condensation nuclei (CCN) on the cloud droplet number concentration and hence the cloud droplet size under the assumption of constant cloud liquid water amount (Twomey, 1974). The second type is called the second aerosol indirect effect (also named "lifetime effect" or "Albrecht effect"), which refers to the microphysically induced effect on the liquid water content, height, lifetime, and precipitation efficiency of clouds due to the aerosol-induced cloud droplet size reduction (Albrecht, 1989). For the first AIE, CDER should decrease, and COD and CWP increase, with increasing AOT (which is considered as a proxy of column aerosol concentration (Hegg & Kaufman, 1998; Kaufman et al., 2005; Loeb & Schuster, 2008; Matheson et al., 2005)). For the second AIE, CCF should increase and precipitation efficiency should decrease with increasing AOT. The aerosol invigoration effect generally refers to the connection between the increase in aerosol loading and the enhanced growth of clouds (Altaratz et al., 2014; Koren et al., 2014; Lebo & Seinfeld, 2011), which can be reflected in a larger cloud cover fraction, greater cloud top height, and an increase in the condensate mass (e.g., CWP and COD) in the atmospheric column.

A typical feature associated with the conventional cloud lifetime effect is the reduced precipitation efficiency (Albrecht, 1989). As a result, precipitation efficiency will be higher in the clean case than in the polluted case, other conditions being the same. Rosenfeld and Gutman (1994) found out from satellite and radar data analysis that a value of 14 μm for CDER (or re) is the threshold for dominant collision and coalescence processes and the separation of precipitating from nonprecipitating clouds. Cloud droplets need to experience longer residence time to grow to 14 μm in a polluted environment than in a clean environment (Rosenfeld & Lensky, 1998; Rosenfeld & Woodley, 2001). Accordingly, we sorted out the water clouds with $r_e \geq 14$ μm and $r_e < 14$ μm from all the water clouds and use the difference of their CTH and CTT [ΔCTH = CTH ($r_e < 14$ μm) − CTH ($r_e \geq 14$ μm) or ΔCTT = CTT ($r_e < 14$ μm) − CTT ($r_e \geq 14$ μm)] as a derived cloud variable for studying precipitation efficiency. This is because with the precipitation efficiency declining with increasing AOT and precipitation being suppressed, cloud droplets need to travel to higher altitude to form precipitation. ΔCTH and ΔCTT are calculated for each individual data points and then averaged for monthly means and other binning processes.

Based on cloud model simulations, aerosol-cloud interaction has been classified into three regimes based predominantly on the response of cloud droplet number concentration to aerosol particle number concentration (or loading) and cloud updraft velocity (Chen et al., 2016; Reutter et al., 2009): (1) aerosol-limited regime in which cloud droplet number concentration is proportional to aerosol particle number concentration (or loading) and nearly independent of cloud updraft velocity, (2) updraft-limited regime in which cloud droplet number concentration is proportional to cloud updraft velocity and nearly independent of aerosol particle number concentration, and (3) transitional regime in which cloud droplet number concentration depends nonlinearly on both aerosol particle number concentration and updraft velocity in cloud.

This study systematically examines the correlation features between AOT (or τ) and the key cloud variables, including CDER (or r_e), COD (or τ_c), CWP, CCF, CTH, CTT, ΔCTH, and ΔCTT, to identify the signatures of aerosol-cloud interaction. Specifically, the linear correlation between AOT and the key cloud variables and the changing trends of these cloud variables with increasing AOT are explored using their long-term averaged monthly mean values. Even though our focus is on identifying the AIE signature in various forms and the corresponding AOT regimes and active regions over the global oceans, the imprints of aerosol invigoration effect are also explored. Long-term averaged (1981–2011) monthly mean values of AOT and the cloud variables, which are less noisy comparing to instantaneous values or short-term averaged values, are used in our correlation analysis to capture more robust AIE signatures from a climatology perspective.

3. Study of Sensitive AIE Regimes

It was found by Shao and Liu (2005) using instantaneous satellite observations that the response of CDER, COD, CWP, and CCF to the increased aerosol loading for marine stratocumulus off the coast of California can be variable, depending on the coupled effects of aerosol loading and macroscale cloud depth

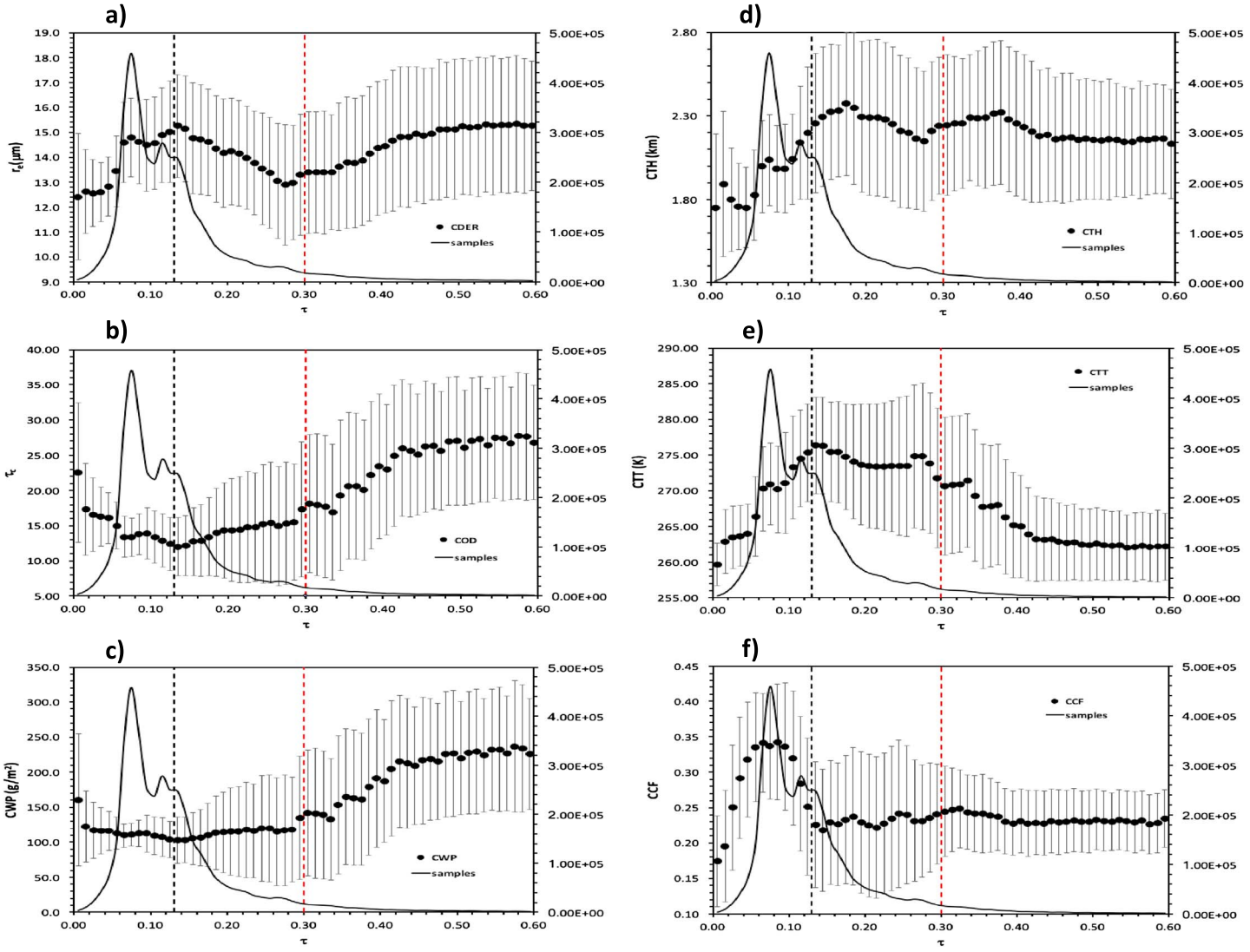

Figure 1. The relationship plot (black dots) of τ (or AOT) versus (a) r_e (or CDER), (b) τ_c (or COD), (c) CWP, (d) CTH, (e) CTT, and (f) CCF for the long-term averaged monthly mean data over the global oceans. The number of data samples (black line) is measured by the vertical coordinate on the right-hand side. The data are binned according to AOT with a 0.01 incremental interval. The error bars indicate the one standard deviation, and the two vertical dashed lines at AOT = 0.13 and 0.30, respectively, are used to divide the plot into three AOT regimes.

(or cloud dynamics/thermodynamics) on cloud droplet sizes. The debate on macrophysical versus microphysics differences for the same region (Lin, Zhang, & Loeb, 2009, 2010; Liu, 2010) raised similar intriguing question. Yuan et al. (2008) also reported that satellite-derived correlation between AOT and CDER, COD, CWP, and CCF can be negative, positive, or neutral, depending on the location and regime of the clouds. Therefore, for the regions where AOT is negatively correlated with CDER from satellite observations, the AIE is manifested and detectable by the satellite observations. If positive correlations of AOT with COD, CWP, and CCF are observed simultaneously in the same regions where AOT correlates negatively with CDER, the AIE detected by CDER reduction in the satellite observation is further manifested in the satellite-observed changes in COD, CWP, and CCF. For the regions with positive or no correlation between AOT and CDER, aerosol-cloud interaction may still occur in unconventional ways (e.g., Koren et al., 2008, 2014; Yuan et al., 2008). Moreover, AIE may also be overridden by the cloud dynamic effect as suggested by Shao and Liu (2005). In this case, the AIE cannot be detected by the satellite observations. Instead of using instantaneous satellite observation, here we identify the AOT regimes in which the conventional aerosol indirect effects are likely to manifest in long-term averaged global monthly mean satellite data of AOT and the cloud variables through the correlation analyses.

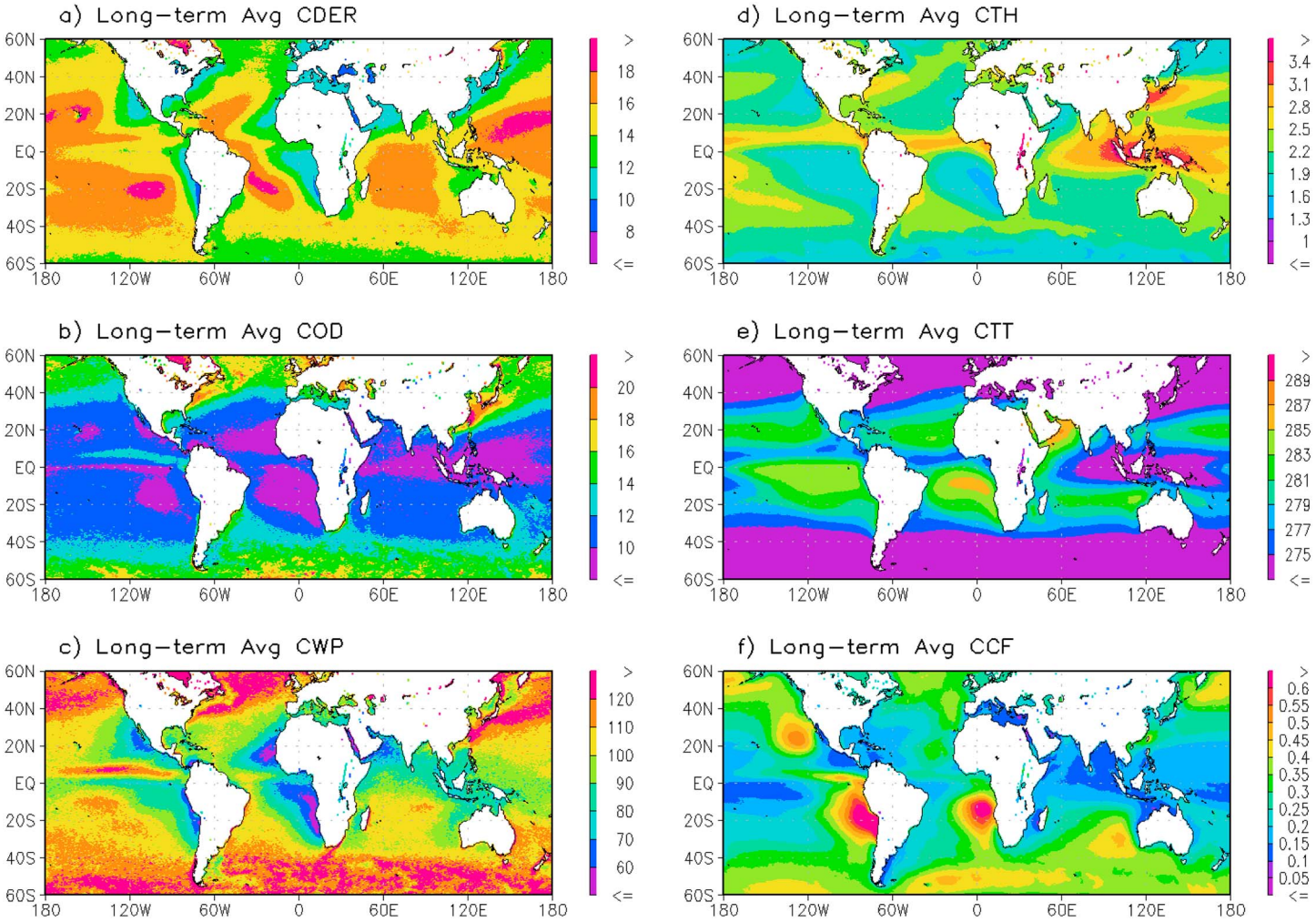

Figure 2. Global distributions of (a) CDER, (b) COD, (c) CWP, (d) CTH, (e) CTT, and (f) CCF for their long-term averaged monthly mean values over the global oceans.

3.1. Statistical Analysis and Results

For the conventional first AIE, AOT should be negatively correlated with CDER and positively correlated with COD and CWP (Coakley et al., 1987; Twomey, 1977), which can be considered as the signature of the first AIE. Figure 1 shows the relationships between the long-term averaged global monthly mean AOT and six cloud variables (CDER, COD, CWP, CTH, CTT, and CCF). The corresponding global distributions of long-term averaged global monthly means for the six cloud variables are plotted in Figure 2. Three regimes can be identified clearly from Figure 1 according to the variations of three key cloud variables (CDER, COD, and CWP) with AOT: (1) Regime I of AOT $<$ 0.13, where CDER increases but COD decreases as AOT increases and CWP decreases rapidly at the beginning then stays nearly constant; (2) Regime II of 0.13 $<$ AOT $<$ 0.3, where CDER decreases but COD and CWP increase as AOT increases; (3) Regime III of AOT $>$ 0.3, where CDER, COD, and CWP first all increase with increasing AOT and then level off. The sampling frequency (solid curve) shows that the majority of the global sample points falls in the first regime and the transition zone from the first regime to the second regime (0.06 $<$ AOT $<$ 0.18). These three regimes can be seen clearer in Figure 3, which shows the scatterplots of averaged CDER versus COD and CWP for the individual AOT bins defined in Figure 1. Black dots are in Regime I, purple and blue dots are in Regime II, and green, yellow, and red dots are in Regime III.

The relationships of CTH, CTT, and CCF to AOT are more complicated due to their strong connections with cloud dynamics and thermodynamics. In Regime I, CTH and CTT generally increase together with increasing AOT. In Regime II, changes of CTH and CTT with AOT are much more complex (see also the purple and blue dots in Figure 4a), which probably suggests that both cloud dynamics and AIE contribute to the changes of

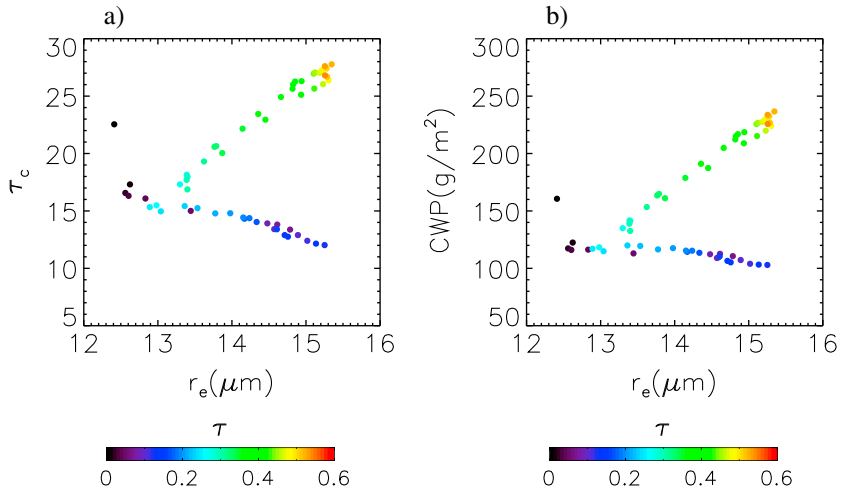

Figure 3. Plot of (a) r_e (or CDER) versus τ_c (or COD) and (b) CDER versus CWP for the mean values of CDER, COD, and CWP in each τ (or AOT) bin defined in Figure 1. The AOT values are color coded for each point.

CTH and CTT. In Regime III, CTH increases but CTT decreases first with AOT; then, they decrease together with further AOT increases and level off eventually at large AOT. CCF first increases with AOT, peaks near the AOT of 0.08, and then decreases with further AOT increases in Regime I. CCF is nearly constant from AOT ~0.13 to ~0.4 along with some minor up-and-down fluctuations. After AOT becomes larger than 0.4, CCF becomes independent from AOT increase. The nonmonotonic behavior of CCF can be seen clearer in the scatterplots of Figures 4b and 4c.

Figure 5a (or Figure 5b) shows the relationship between AOT and ΔCTH (or ΔCTT) for their long-term averaged global monthly mean values. When AOT increases from 0 to 0.14, ΔCTH (ΔCTT) decreases (increases) from positive (negative) to negative (positive). ΔCTH (ΔCTT) stays negative (positive) but nearly constant (in their highest magnitude) in the range of $0.14 < \text{AOT} < 0.27$. They reverse back to increase (or decrease) from negative (or positive) to positive (negative) beyond $\text{AOT} > 0.27$ and level off eventually at very large AOT values. The changes of ΔCTH (or ΔCTT) with increasing AOT can be seen clearer in the scatterplot of Figure 5c (or Figure 5d).

3.2. Explanations and Discussions

Regime I where aerosol loading increases from a pristine atmosphere to an atmosphere with slightly increased aerosol particles (e.g., sea salt) falls into the aerosol-limited regime whereby the microphysical

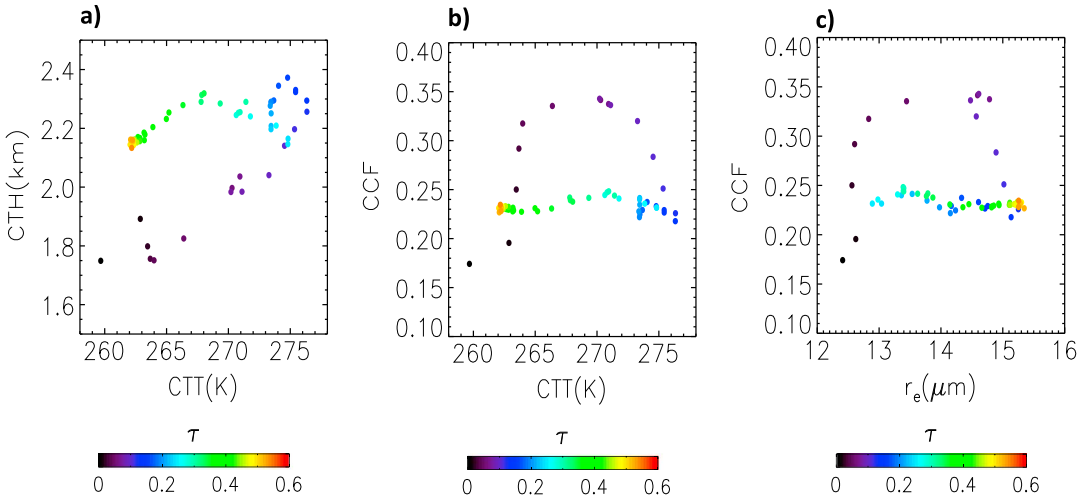

Figure 4. Similar to Figure 3 but for (a) CTH versus CTT, (b) CCF versus CTT, and (c) CCF versus r_e (or CDER).

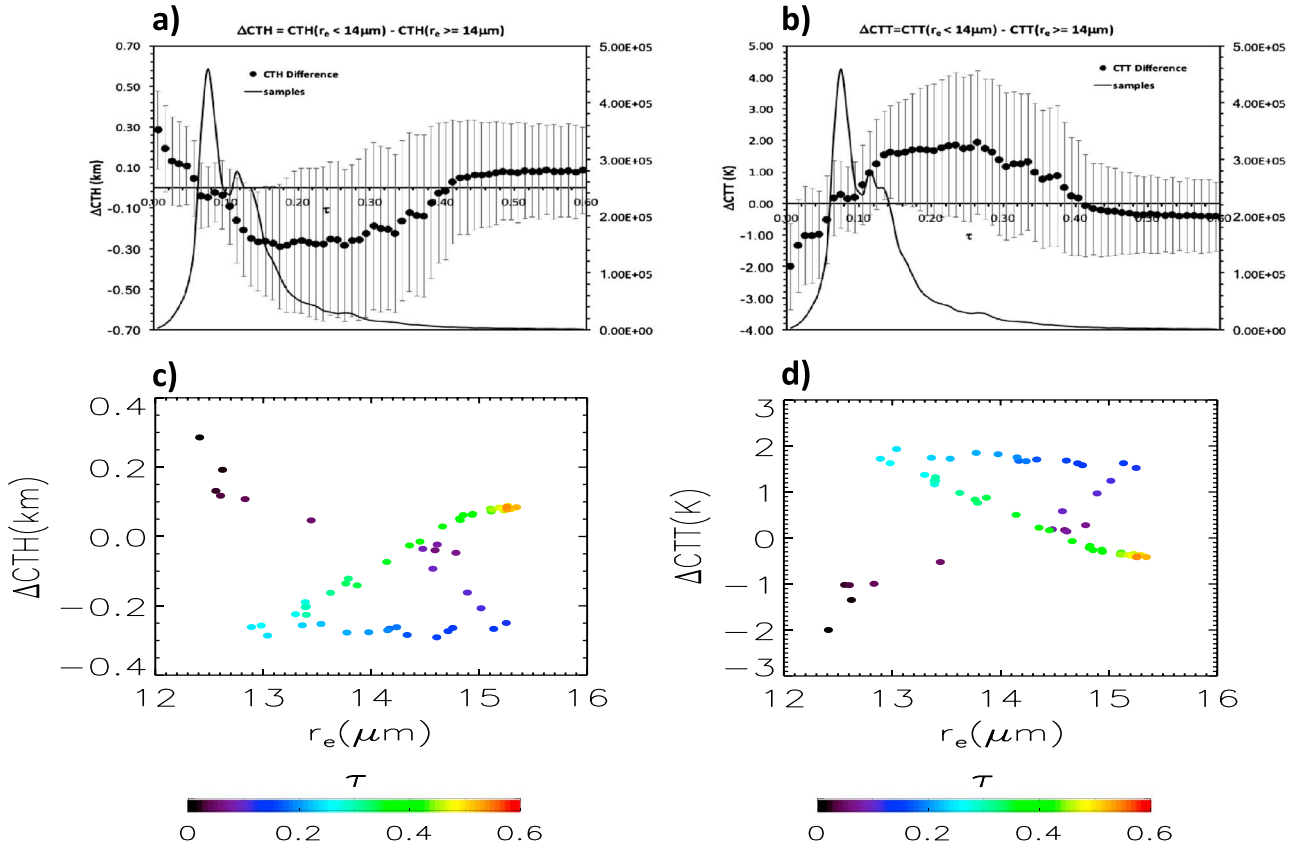

Figure 5. Top two panels are similar to Figure 1 but for τ (or AOT) versus (a) ΔCTH and (b) ΔCTT. Bottom two panels are similar to Figure 3 but for r_e (or CDER) versus (c) ΔCTH and (d) ΔCTT. ΔCTH = CTH ($r_e < 14$ μm) − CTH ($r_e \geq 14$ μm) and ΔCTT = CTT ($r_e < 14$ μm) − CTT ($r_e \geq 14$ μm).

cloud development is mainly controlled by the availability of cloud condensation nuclei (CCN) originated from aerosols (see Chen et al., 2016; Reutter et al., 2009). When AOT starts increasing in a pristine environment, since the number of cloud droplets involved in the competition for water vapor are still limited, the latent heat released from increasing condensational growth strengthens the cloud growth, as indicated by the increase of CTH with increasing AOT (see Figures 1d and 4a) due to the aerosol invigoration effect identified by Koren et al. (2014) as an extension of the concept of aerosol-limited clouds. Thus, as AOT increases, clouds grow higher and the growth of cloud droplets lasts longer in the clouds. The thicker and stronger clouds also allow cloud droplets to grow to the size that triggers collision/coalescence processes, which results in less cloud droplet concentration but bigger droplet size and enhances CDER increase along with COD decrease. CWP starts to decrease slightly when rain is initiated for CDER larger than 14 μm (see Figure 3b). The concurrent increase of CCF with increasing AOT and opposite variations of CTH and CTT suggest that the clouds at the low AOT end in Regime I are capped by the temperature inversions of marine boundary layer (MBL). The relatively low values of both CTH and CTT in Regime I (see Figures 2d and 2e) further indicate that the corresponding regions of this regime are mainly located over the remote oceans of middle/high latitudes in both hemispheres.

The behavior of CCF is more interesting: CCF increases first with increasing AOT when AOT is lower than 0.08 due to the aerosol invigoration effect in a pristine environment (Koren et al., 2014; Twomey & Squires, 1959). When AOT increases from 0.08 to 0.13, clouds further grow to higher altitudes (see Figure 1d) and cloud droplets also grow to larger than 14 μm (see Figures 1a and 4c). This suggests, at the high AOT end of Regime I (AOT $>$ 0.08), that cloud droplets grow large enough due to collision/coalescence processes (Liu et al., 2006; Liu et al., 2004) and fall out as a rain, leading to dissipation of clouds. The decreasing (increasing) trend of ΔCTH (ΔCTT) with AOT increase in Regime I suggests that the precipitation efficiency is suppressed since precipitation initiates at a higher altitude for a larger AOT value. The collective results suggest that Regime I likely

corresponds to the aerosol-limited regime (Chen et al., 2016; Reutter et al., 2009) coupled with the aerosol invigoration effect (Koren et al., 2014).

In Regime II, more activated aerosols participate in the competition for water vapor so that their growth to larger cloud droplets is suppressed. As a result, when AOT increases, CDER decreases, COD increases, and CWP slightly increases due to more small cloud droplets. CTH/CTT slightly increases/decreases first with increasing AOT and slowly decreases/increases thereafter, but their values are still high and relatively stable probably due to the comparable competing effect of cloud microphysical and macrophysical processes. CCF stays nearly constant with some minor fluctuations resulting probably from the competitions among the AIE, precipitation dissipation, and cloud macrophysics (such as entrainment/detrainment). Since ΔCTH(ΔCTT) maintains the largest negative (positive) value with little changes with AOT increase in most part of the regime (except at the low and high ends of AOT), the inhibition of precipitation efficiency becomes saturated after reaching the maximal at the beginning of the regime and stays unchanged until AOT further increases into Regime III. The correlation observed in this regime for AOT and the cloud variables matches the basic features of the conventional aerosol indirect effects so that this second regime is considered as the sensitive regime of the conventional AIEs. In other words, the conventional AIEs are manifested in this regime in the form of CDER (COD) decreasing (increasing) with AOT increasing, while CWP displays slightly increasing trend along with nearly constant cloud cover and suppressed precipitation. This regime is associated likely with the transitional regime between the aerosol-limited Regime I (see the discussion above) and the updraft-limited Regime III (see the discussion below).

Regime III exhibits distinct behaviors of concurrent increases of CDER, COD, and CWP with increasing AOT, warranting more discussions. Note that this regime starts with CDER close to 13 μm (nonprecipitation droplets) and ends with CDER larger than 15 μm (precipitation droplets) (see Figure 4c), along with increasing CTH with increasing AOT at the beginning of the regime, which suggests a cloud development due to aerosol invigoration at high AOT. Changes in aerosol loading can be linked to changes in buoyance through latent heating and consequently vertical velocity (Lebo & Seinfeld, 2011). According to the mechanism proposed by Stevens and Feingold (2009), more smaller droplets due to higher aerosol loading delay the onset of precipitation. This allows cloud droplets to be carried to higher levels, increasing the amount of condensed water within the cloud, in turn increasing evaporation at cloud top and moistening/cooling the layer above the cloud, hence destabilizing the cloud top region. As a result, updrafts near cloud top are invigorated and cloud depth increases along with enhanced microphysical collection processes. Invigorated clouds at high AOT grow higher and lead to larger CDER near the cloud top, contrasting the direct aerosol-induced decrease of CDER in Regime II. Thus, the CDER (or r_e) behavior resulted likely from combined aerosol effects on droplet concentration and cloud thickness can be briefly expressed as

$$r_e = \left(\frac{3}{4\pi\rho_w}\right)^{1/3} \beta \left(\frac{L}{N}\right)^{1/3} = \left(\frac{3}{4\pi\rho_w}\right)^{1/3} \beta \left(\frac{cH}{N}\right)^{1/3}. \quad (1)$$

where the nondimensional parameter β is an increasing function of relative dispersion (Liu & Daum, 2000), L is liquid water content, c is related to cloud base properties that can be roughly assumed constant, H is cloud thickness, and N is droplet concentration. When aerosol increases, both N and H increase so that whether the retrieved r_e increases or decreases with increasing AOT depends on the balance between the two effects. An increasing r_e could mean that increasing H outweights the increasing N, and this is probably true due to the invigoration. Further, it has been found that in addition to droplet concentration, relative dispersion also changes with aerosol properties and results in the so-called dispersion effect (Chen et al., 2016; Liu & Daum, 2002). Deeper clouds are expected to have more liquid water and an increase in precipitation is expected, which may explain the enhancement of precipitation efficiency suggested by the decrease (increase) of ΔCTH (ΔCTT) with increasing AOT at the beginning of Regime III. The dispersion effect may also contribute to the enhancement of precipitation efficiency, especially in the regions influenced by larger aerosol particles (such as sea salt and dust particles). The feature of high CTH corresponding to small CTT in Figures 1d and 1e in this regime suggests that the corresponding regions of Regime III are over the tropical convergence zones by examining the distributions of CTH and CTT in Figures 2d and 2e, where cloud dynamics is likely intensive so that the increasing H should outweight the increasing N in addition to the invigoration effect. As a result, the conventional AIEs are

obscured completely. It is noteworthy that although the high aerosol loading appears to suggest that Regime III corresponds likely to the updraft-limited regime, the concurrent strong convection adds some uncertainties to this conclusion and more researches are needed.

4. The AIE Active Regions

A follow-up question is where those AIE sensitive regimes are located over the global oceans. To answer this question, the linear correlations between AOT and the cloud variables have been calculated for 2.5° × 2.5° spatial grid over global oceans using their long-term averaged monthly mean values in 0.1° × 0.1° spatial resolution and analyzed in this section. The selection of 2.5° × 2.5° spatial grid is consistent with that used by Sekiguchi et al. (2003) for a similar statistics analysis of AIEs over the global oceans using 1 year satellite observation.

4.1. The First AIE Active Regions

The global distributions of the slope of $\log_{10}$(AOT) versus $\log_{10}$(CDER), $\log_{10}$(COD), and $\log_{10}$(CWP) are shown in Figures 6a–6c, respectively. The contours indicate that the obtained linear correlation slope is above 95% confidence level. Distinct negative slope with confidence level higher than 95% of log10(AOT) versus log10(CDER) is observed over several oceanic regions in middle and low latitudes: (a) a swath extending from the east coast of China to the North Pacific Ocean at about 20°N–40°N latitudes (CH-NPO hereafter), (b) a swath extending from the east coast of USA to the North Atlantic Ocean at about 25°N–35°N latitudes (US-NAO), (c) the southern end of Arabian Sea (SAS), (d) tropical and subtropical Atlantic Ocean extending from the west coast of North and Central Africa to the east coast of Central America (Tro-AO), (e) a belt area extending from the west coast of South America to about 130°W longitude at about ~10°S of tropical South Pacific Ocean (Tro-SPO), and (f) a long narrow region along the west coast of central South America (WcSAm). These six areas extending from the coastal oceans under the influence of offshore continental aerosols to the remote oceans will be further examined below.

To further confirm the first AIE signature revealed by the clear negative correlation between AOT and CDER in the above six regions, a distinct positive slope of $\log_{10}$(AOT) versus $\log_{10}$(COD) and $\log_{1}$(AOT) versus $\log_{10}$(CWP) is also likely to be obtained for the regions. This is only true for the regions of CH-NPO, US-NAO, and WcSAm. For the first AIE, a negative correlation between CDER and COD should also hold, which is indeed the case in the three regions of CH-NPO, US-NAO, and WcSAm as shown in Figure 6d (the global distribution of the slope for the linear correlation of CDER versus COD). Thus, it is concluded that the first AIE only manifests in the three regions of CH-NPO, US-NAO, and WcSAm for the three cloud variables (CDER, COD, and CWP) from a climatology perspective. For the other three regions (SAS, Tro-AO, and Tro-SPO) with negative correlation between AOT and CDER, either correlation between AOT and COD (CWP) is not positive or correlation between CDER and COD is not negative; the first AIE is only manifested in CDER but concealed probably by other cloud microphysical or dynamical processes for the other cloud variables (COD and CWP). This suggests that cloud droplet size is more susceptible to the first AIE than the other cloud variables.

Actually, SAS, Tro-AO, and Tro-SPO are in either the tropical uplifting zones or the corresponding subsidence zones over the south and north subtropical oceans so that cloud dynamic processes are active and prominent. The effect of the active cloud dynamic processes entangles with the AIE and overrides it in the changes of COD and CWP. The evident positive correlation between AOT and the three cloud variables (CDER, COD, and CWP) in the tropical convergence zones is mainly the signature of cloud updraft dynamic effect, which totally obscured the signature of the first AIE in a sense of long-term average (or climatology).

4.2. The Second AIE Active Regions

The global distribution of long-term averaged monthly mean CCF and the slope of $\log_{10}$(AOT) versus CCF are shown in Figure 7 (Figure 2f is replotted as Figure 7a for an easy comparison with Figure 7b). Regions with higher CCF of warm water clouds are located in several oceanic areas near the west coasts of the continents, such as California/Mexico, central South America, South Europe/North Africa, South Africa, and Australia along with the southeast coast of China. Positive correlation between AOT and CCF is also evident in these regions with much more reduced spatial coverage, which indicates that the second AIE is likely to manifest

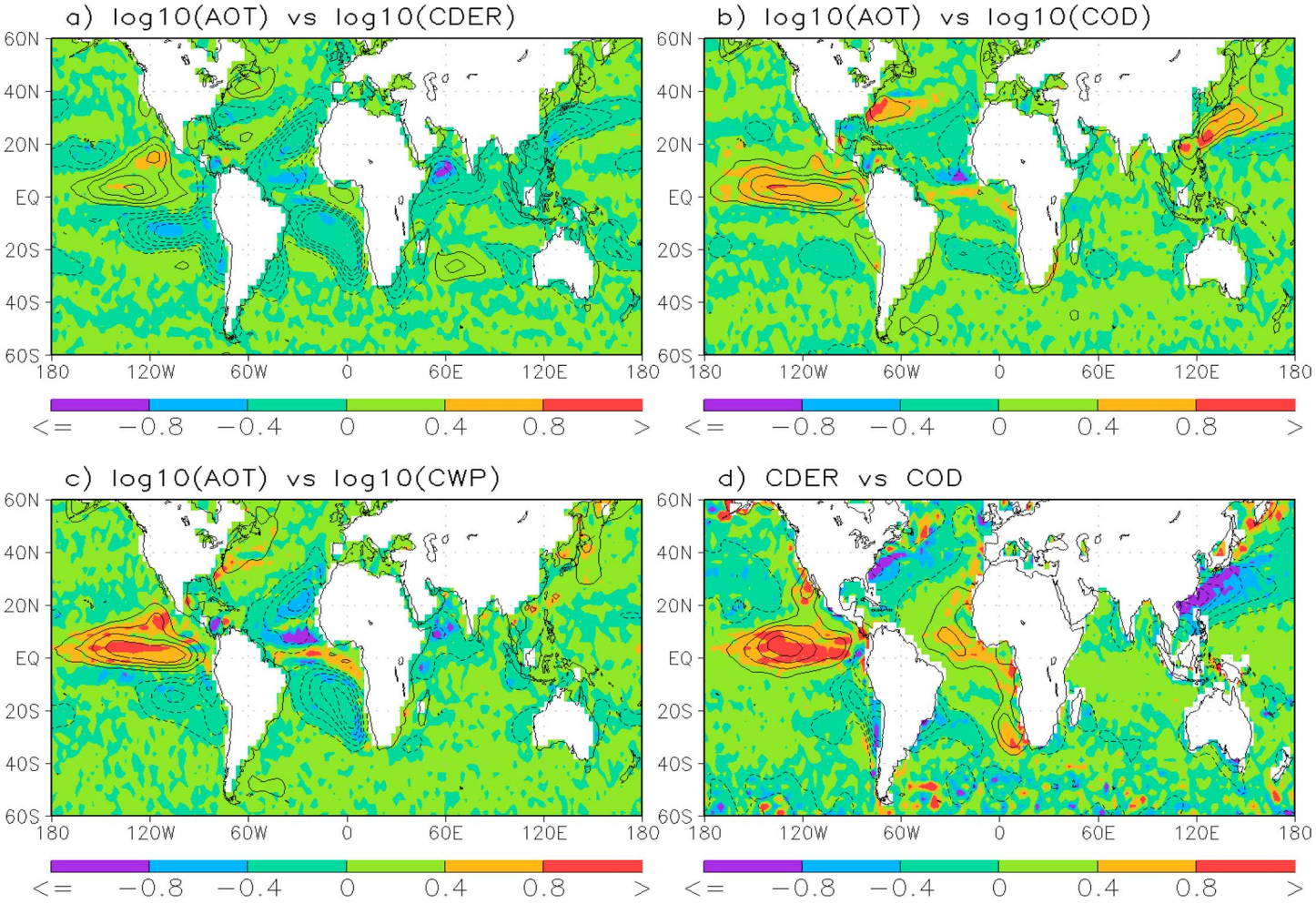

Figure 6. Global distributions of the slope of linear correlation between (a) $\log_{10}$(AOT) and $\log_{10}$(CDER), (b) $\log_{10}$(AOT) and $\log_{10}$(COD), (c) $\log_{10}$(AOT) and $\log_{10}$(CWP), and (d) CDER and COD. The areas where the confidence level of linear correlation slope is above 95% are marked by the contours. The linear correlation is calculated for 2.5° × 2.5° spatial grids over the global oceans using the long-term averaged monthly mean values in 0.1° × 0.1° spatial resolution.

in these regions. Distinct positive correlation is also observed in the tropical convergence zones, whereas negative correlation is observed in the corresponding subsidence zones over the subtropical oceans, which is mainly a signature of cloud dynamic effect rather than the signature of the second AIE in view of the strong uplifting (or descending) air motion in these remote oceanic zones. Regions with higher CCF of supercooled water clouds are located mainly in the areas with active synoptic storms at the high latitudes of both hemispheres, where the second AIE signature is vague since there are barely any evident positive correlations between AOT and CCF. The synoptic cloud dynamics probably overpowers the AIE and determines the cloud behaviors in the storm active regions.

Figure 8 displays the global distribution of long-term averaged monthly mean ΔCTH and AOT. It is interesting to note that the patterns (see Figure 8a) with negative ΔCTH over the oceanic regions influenced by the aerosols from offshore dust (e.g., the west coast of North Africa and Arabian Sea), industrial pollution (e.g., the east coast of USA, China, and Bay of Bangle), and biomass burning (e.g., the west coast of Central/South Africa and the oceanic regions of South East Asia) are very similar to the higher AOT distribution patterns (see Figure 8b) of these offshore aerosols, which suggest a declined precipitation efficiency.

Figure 9 shows CTT and CDER relationship for four rectangle oceanic regions (which are marked by the four red boxes in Figure 8b) with four typical aerosol scenarios: region 1 (−130°W, −120°W; 30°N, 40°N) is with slightly polluted air over the west coast of California, region 2 (120°E, 130°E, 20°N, 30°N) is with polluted air over the east coast of China, region 3 (−170°W, −90°W; −50°S, −40°S) is with clean air over the South

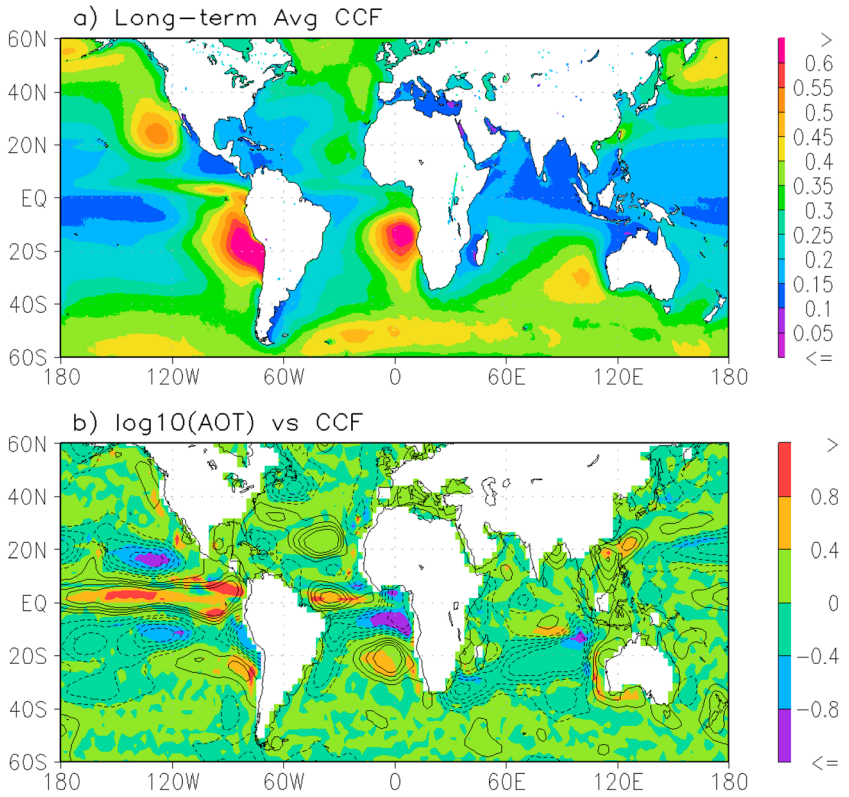

Figure 7. Global distributions of (a) CCF and (b) the slope of linear correlation between $\log_{10}$(AOT) and CCF for the long-term averaged monthly mean values. The areas where the confidence level of linear correlation slope is larger than 95% are marked by the contours. The linear correlation is calculated for 2.5° × 2.5° spatial grids over the global oceans using the original data in 0.1° × 0.1° spatial resolution.

Pacific Ocean, and region 4 (−30°W, −20°W; 10°N, 20°N) is dominated by dust plume from North Africa. Monthly mean CTT of 372 months from 1981 to 2011 has been plotted versus the corresponding CDER for the four selected regions. It is interesting to note the following: (1) most of the cloud droplets in region 3 with clean air can grow up to larger than 14 μm and become rain after traveling a sufficient distance vertically; (2) it is hard for the cloud droplets to grow up to larger than 14 μm in region 2 or region 4 with polluted or dusty air; and (3) there are still some cloud droplets that can grow up to larger than 14 μm in region 1 with slightly polluted air after traveling a sufficient distance vertically. These results suggest that aerosol pollution does reduce the precipitation efficiency and suppresses the precipitation of marine water clouds in a sense of long-term perspective over broader oceanic regions influenced by the offshore continental aerosols.

It is also interesting to see if there is any direct relationship between the first and second AIE in a sense of long-term average. It is seen from Figure 2a that CDER gradually decreases from remote oceanic regions (with the values larger than 14 μm) to the coastal oceanic regions (with the values in the range of 10–13 μm) due to the first AIE from the offshore continental aerosols. There are also evident negative correlations between AOT and ΔCTH over the oceanic regions influenced by the offshore continental aerosols as shown in Figure 8. However, there are very low correlations between CDER and CCF (or ΔCTH) over the global oceans as shown in Figure 10 (the distribution for the slope of the linear correlation of CDER versus CCF and ΔCTH, respectively). Considering that the first AIE does manifest in the CDER reduction and the second AIE also manifests in the CCF increase and precipitation efficiency decline in some common oceanic regions, lacking of clear correlation between CDER and CCF (or ΔCTH) suggests solely that CDER reduction due to the aerosol and cloud interaction is not sufficient for the subsequent occurrence of the second AIE and proper cloud dynamic conditions are necessary for the aerosol and cloud interaction to evolve from the stage of the first AIE to the second AIE.

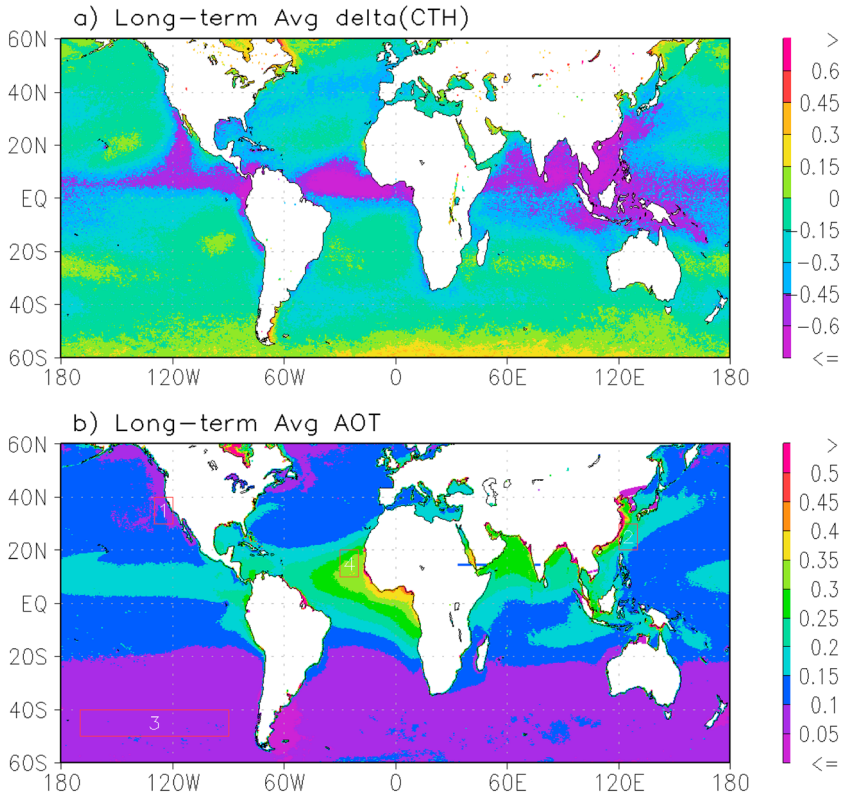

Figure 8. Global distributions of (a) ΔCTH and (b) AOT for their long-term averaged monthly mean values. The four regions marked by the four red rectangle boxes in the bottom panel are used for Figure 9.

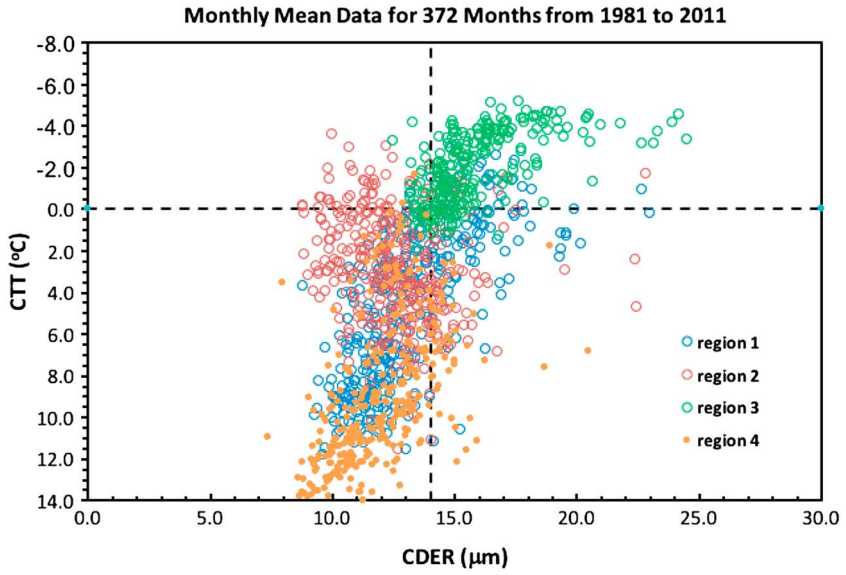

Figure 9. Scatterplot of regionally averaged monthly mean CTT versus CDER for 372 months from 1981 to 2011 in four selected regions with different aerosol loading scenarios. Regions 1, 2, 3, and 4 (marked by the four red rectangle boxes in Figure 8b) are with slightly polluted aerosol loading, high polluted aerosol loading, high dust aerosol loading, and clean marine air, respectively. The vertical dash line is set for CDER equals 14 μm (low threshold of precipitation droplets), and the horizontal dash line is set for CTT equals 0°C (melting point of water).

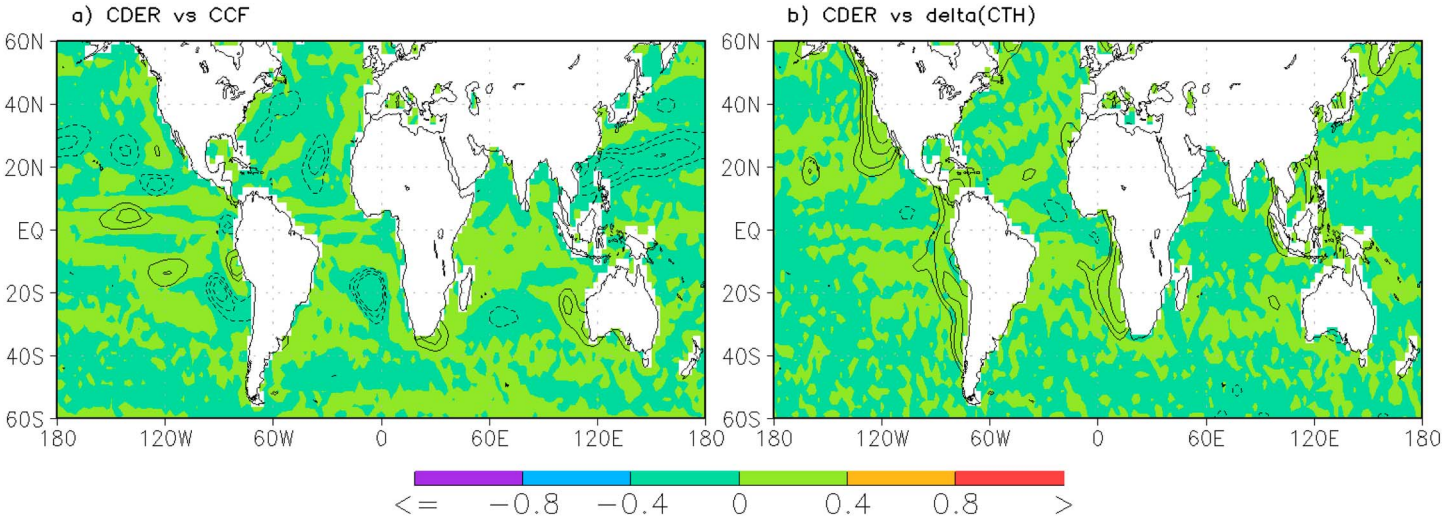

Figure 10. Global distributions of (a) the slope of linear correlation between CDER and CCF and (b) CDER and ΔCTH for the long-term averaged monthly mean values. The areas where the confidence level of linear correlation slope is larger than 95% are marked by the contours. The linear correlation is calculated for 2.5° × 2.5° spatial grids over the global oceans using the original data in 0.1° × 0.1° spatial resolution.

5. Summary and Conclusions

Long-term satellite AVHRR CDRs of cloud and aerosol have been used to investigate the AIE of marine water cloud from the perspective of climatology. Identifying the AOT regimes and geolocations where the AIE may manifest clearly in a sense of long-term average over the global oceans is the focus of this study.

Three regimes based on AOT have been found for the response of CDER, COD, and CWP to the changes of aerosol loading in view of global long-term average. In the first regime (AOT $<$ 0.13), CDER/COD increases/decreases with AOT increases and CWP decreases slightly with AOT increases. This regime mainly falls in the remote oceanic regions with moist and pristine atmosphere at middle/high latitudes, which favors the set off of the aerosol invigoration effect in the aerosol-limited regime.

The conventional first AIE manifests clearly in the form of CDER/COD decreasing/increasing with AOT increasing, while CWP keeps minor increasing trend in the second regime (0.13 $<$ AOT $<$ 0.3). As a result, the second regime can be considered as the sensitive regime of the conventional first AIE, which can be considered as a transition regime from the aerosol-limited regime to the updraft-limited regime identified in the cloud model simulations. The aerosol and cloud microphysical processes are dominant in this regime comparing to the cloud macrophysical processes so that the first AIE signature is not obscured by the cloud dynamics and detectable in the long-term averaged observations.

In the last regime (AOT $>$ 0.3), CDER, COD, and CWP first increase together due to the cloud development invigorated by high aerosol loading and large sea salt/dust particles and then level off toward the end of the regime, where cloud macrophysics becomes dominant. As a result, the AIE signatures are obscured and hard to be detected in the observation. The first AIE manifests itself in the reduction of CDER over the global coastal oceans where offshore aerosols that originated from land sources are prevailed. Six oceanic regions, CH-NPO, US-NAO, SAS, Tro-AO, Tro-SPO, and WcSAm, have been identified as the first AIE active regions revealed in the CDER change, but only in three of them (CH-NPO, US-NAO, and WcSAm) the first AIE is revealed in a consistent change of three cloud variables (CDER, COD, and CWP). The signature of the first AIE manifested in CDER is more evident, and spatial coverage is also broader than that in COD and CWP, which indicates that CDER is more susceptible to the aerosol-cloud interaction than COD and CWP.

Distinct increase of CCF induced by aerosol is only identified for relatively low AOT ($<$0.08) regime in a sense of global long-term average due to the aerosol invigoration of clouds in moist and clean air over remote oceans. The regions that the second AIE is likely to be detected in the CCF increase are in several oceanic areas near the west coasts of the continents with higher CCF of warm water clouds, including California/Mexico, central South America, South Europe/North Africa, South Africa, and Australia along with the east coast of China.

The second AIE signature revealed in the decline of the precipitation efficiency represented by the change of ΔCTH (or ΔCTT) with increasing AOT is detectable in the AOT regime of $0.08 < \text{AOT} < 0.4$. The corresponding oceanic regions are mainly in the downwind oceanic areas of the continental aerosols. Solely the CDER reduction due to aerosol-cloud interaction is not sufficient for the interaction to evolve from the stage of the first AIE to the second AIE, and proper cloud dynamic conditions are necessary to maintain the evolution. More researches from both modeling and observation are needed in the future to identify these proper cloud dynamics conditions. The results of this study based on the long-term averaged satellite observation are valuable for the evaluation and improvement of the AIE in global climate models, which are only evaluated and assessed so far against instantaneous or short-term averaged observations of the AIE.

It is noteworthy that Liu and Daum (2002) reported that increased aerosols can alter the spectral shape of the cloud droplet size distribution and exerts a dispersion effect that acts to offset the cooling from increased droplet concentration (or β swelling effect in equation (1)). Subsequent studies have found that the dispersion effect can be either warming or cooling depending on whether or not the AIE is in aerosol-limited or updraft-limited regimes (Chen et al., 2016, and references therein). Another factor warranting further investigation is the effect of covarying meteorology. Studying these issues from the perspective of long-term average of satellite observations along with model simulations will be our future works.

Appendix: Acronyms

AIE(s)	: aerosol indirect effect(s)
AOT	: aerosol optical thickness
AVHRR	: advanced very high resolution radiometer
CCF	: cloud cover fraction
CCN(s)	: cloud condensation nuclei(s)
CDER	: cloud droplet effective radius
CDR(s)	: climate data record(s)
COD	: cloud optical depth
CTH	: cloud top height
CTT	: cloud top temperature
CWP	: cloud water path
GAC	: global area coverage
IPCC	: Intergovernmental Panel on Climate Change
MBL	: marine boundary layer
MODIS	: Moderate Resolution Imaging Spectroradiometer
NOAA	: National Oceanic and Atmospheric Administration
PATMOS-x	: Pathfinder Atmospheres-Extended

Acknowledgments
The authors (X. Zhao and A. Heidinger) would like to acknowledge the support from the CDR program at the National Centers for Environmental Information (NCEI) of NOAA/NESDIS. Y. Liu is supported by the Department of Energy's Atmospheric System Research (ASR) program. F. Yu acknowledges funding support from the National Aeronautics and Space Administration (NASA NNX17AG35G). The comments and suggestions from three anonymous reviewers and JGR-Atmosphere Editor are constructive for the improvement of the paper. The data used in this paper are archived at the NOAA environment information data center and can be accessed at https://www.ncdc.noaa.gov/cdr/atmospheric/avhrr-aerosol-optical-thickness and https://www.ncdc.noaa.gov/cdr/atmospheric/avhrr-cloud-properties-patmos-x. The views, opinions, and findings contained in this paper are those of the author(s) and should not be construed as an official National Oceanic and Atmospheric Administration or U.S. Government position, policy, or decision.

References

Albrecht, B. A. (1989). Aerosols, cloud microphysics, and fractional cloudiness. *Science*, *245*(4,923), 1227–1230. https://doi.org/10.1126/science.245.4923.1227

Altaratz, O., Koren, I., Remer, L. A., & Hirsch, E. (2014). Cloud invigoration by aerosols—Coupling between microphysics and dynamics. *Atmospheric Research*, *140*, 38–60.

Breon, F. M., Tanre, D., & Generoso, S. (2002). Aerosol effect on cloud droplet size monitored from satellite. *Science*, *295*(5556), 834–838. https://doi.org/10.1126/science.1066434

Cao, C., Weinreb, M., & Xu, H. (2004). Predicting simultaneous nadir overpasses among polar-orbiting meteorological satellites for the intersatellite calibration of radiometers. *Journal of Atmospheric and Oceanic Technology*, *21*, 537–542. https://doi.org/10.1175/1520-0426(2004)021%3C0537:PSNOAP%3E2.0.CO;2

Cao, C. Y., Xiong, X. X., Wu, A. H., & Wu, X. Q. (2008). Assessing the consistency of AVHRR and MODIS L1B reflectance for generating fundamental climate data records. *Journal of Geophysical Research*, *113*, D09114. https://doi.org/10.1029/2007JD009363

Charlson, R. J., Schwartz, S. E., Hales, J. M., Cess, R. D., Coakley, J. A., Hansen, J. E., & Hofmann, D. J. (1992). Climate forcing by anthropogenic aerosols. *Science*, *255*(5043), 423–430. https://doi.org/10.1126/science.255.5043.423

Chen, J. Y., Liu, Y. G., Zhang, M. H., & Peng, Y. R. (2016). New understanding and quantification of the regime dependence of aerosol-cloud interaction for studying aerosol indirect effects. *Geophysical Research Letters*, *43*, 1780–1787. https://doi.org/10.1002/2016GL067683

Coakley, J. A., Bernstein, R. L., & Durkee, P. A. (1987). Effect of ship-stack effluents on cloud reflectivity. *Science*, *237*(4818), 1020–1022. https://doi.org/10.1126/science.237.4818.1020

Hegg, D. A., & Kaufman, Y. J. (1998). Measurements of the relationship between submicron aerosol number and volume concentration. *Journal of Geophysical Research*, *103*(D5), 5671–5678. https://doi.org/10.1029/97JD03652

Heidinger, A. K., Cao, C., & Sullivan, J. T. (2002). Using Moderate Resolution Imaging Spectrometer (MODIS) to calibrate advanced very high resolution radiometer reflectance channels. *Journal of Geophysical Research*, *107*(D23), 4702. https://doi.org/10.1029/2001JD002035

Heidinger, A. K., Straka, W. C., Molling, C. C., Sullivan, J. T., & Wu, X. Q. (2010). Deriving an inter-sensor consistent calibration for the AVHRR solar reflectance data record. *International Journal of Remote Sensing*, *31*, 6493–6517. https://doi.org/10.1080/01431161.2010.496472

Heidinger, A. K., Foster, M. J., Walther, A., & Zhao, X. P. (2014). The Pathfinder atmospheres—Extended AVHRR climate dataset. *Bulletin of the American Meteorological Society*, *95*(6), 909. https://doi.org/10.1175/Bams-D-12-00246.1

Ignatov, A., & Stowe, L. (2002). Aerosol retrievals from individual AVHRR channels. Part I: Retrieval algorithm and transition from Dave to 6S radiative transfer model. *Journal of the Atmospheric Sciences*, *59*(3), 313–334.

Intergovernmental Panel on Climate Change (IPCC) (2014). Climate Change 2014: Mitigation of climate change, *Climate Change 2014: Mitigation of Climate Change*, 1-1435.

Kaufman, Y. J., Koren, I., Remer, L. A., Rosenfeld, D., & Rudich, Y. (2005). The effect of smoke, dust, and pollution aerosol on shallow cloud development over the Atlantic Ocean. *Proceedings of the National Academy of Sciences of the United States of America*, *102*, 11,207–11,212. https://doi.org/10.1073/pnas.0505191102

Koren, I., Martins, J. V., Remer, L. A., & Afargan, H. (2008). Smoke invigoration versus inhibition of clouds over the Amazon. *Science*, *321*, 946–949. https://doi.org/10.1126/science.1159185

Koren, I., Dagan, G., & Altaratz, O. (2014). From aerosol-limited to invigoration of warm convective clouds. *Science*, *344*(6,188), 1143–1146. https://doi.org/10.1126/science.1252595

Lebo, Z. J., & Seinfeld, J. H. (2011). Theoretical basis for convective invigoration due to increased aerosol concentration. *Atmospheric Chemistry and Physics*, *11*, 5407–5429.

Lin, W. Y., Zhang, M. H., & Loeb, N. G. (2009). Seasonal variation of the physical properties of marine boundary layer clouds off the California coast. *Journal of Climate*, *22*, 2624–2638. https://doi.org/10.1175/2008JCLI2478.1

Lin, W. Y., Zhang, M. H., & Loeb, N. G. (2010). Reply to comments on "Seasonal variation of the physical properties of marine boundary layer clouds off the California coast". *Journal of Climate*, *23*, 3421–3423. https://doi.org/10.1175/2010JCLI3483.1

Liu, Y. G. (2010). Comments on "Seasonal variation of the physical properties of marine boundary layer clouds off the California coast". *Journal of Climate*, *23*, 3416–3420. https://doi.org/10.1175/2010JCLI3407.1

Liu, Y. G., & Daum, P. H. (2000). Spectral dispersion of cloud droplet size distributions and the parameterization of cloud droplet effective radius. *Geophysical Research Letters*, *27*(13), 1903–1906. https://doi.org/10.1029/1999GL011011

Liu, Y. G., & Daum, P. H. (2002). Anthropogenica erosols—Indirect warming effect from dispersion forcing. *Nature*, *419*(6,907), 580–581. https://doi.org/10.1038/419580a

Liu, Y. G., Daum, P. H., & McGraw, R. (2004). An analytical expression for predicting the critical radius in the autoconversion parameterization. *Geophysical Research Letters*, *31*, L06121. https://doi.org/10.1029/2003GL019117

Liu, Y. G., Daum, P. H., McGraw, R., & Miller, M. (2006). Generalized threshold function accounting for effect of relative dispersion on threshold behavior of autoconversion process. *Geophysical Research Letters*, *33*, L11804. https://doi.org/10.1029/2005GL025500

Loeb, N. G., & Schuster, G. L. (2008). An observational study of the relationship between cloud, aerosol and meteorology in broken low-level cloud conditions. *Journal of Geophysical Research*, *113*, D14214. https://doi.org/10.1029/2007JD009763

Matheson, M. A., Coakley, J. A., & Tahnk, W. R. (2005). Aerosol and cloud property relationships for summertime stratiform clouds in the northeastern Atlantic from Advanced Very High Resolution Radiometer observations. *Journal of Geophysical Research*, *110*, D24204. https://doi.org/10.1029/2005JD006165

Pavolonis, M. J., Heidinger, A. K., & Uttal, T. (2005). Daytime global cloud typing from AVHRR and VIIRS: Algorithm description, validation, and comparisons. *Journal of Applied Meteorology*, *44*, 804–826.

Ramanathan, V., Crutzen, P. J., Kiehl, J. T., & Rosenfeld, D. (2001). Atmosphere—Aerosols, climate, and the hydrological cycle. *Science*, *294*(5,549), 2119–2124. https://doi.org/10.1126/science.1064034

Reutter, P., Su, H., Trentmann, J., Simmel, M., Rose, D., Gunthe, S. S., … Poschl, U. (2009). Aerosol- and updraft-limited regimes of cloud droplet formation: influence of particle number, size and hygroscopicity on the activation of cloud condensation nuclei (CCN). *Atmospheric Chemistry and Physics*, *9*(18), 7067–7080.

Rosenfeld, D., & Gutman, G. (1994). Retrieving microphysical properties near the tops of potential rain clouds by multispectral analysis of AVHRR data. *Atmospheric Research*, *34*(1–4), 259–283. https://doi.org/10.1016/0169-8095(94)90096-5

Rosenfeld, D., & Lensky, I. M. (1998). Satellite-based insights into precipitation formation processes in continental and maritime convective clouds. *Bulletin of the American Meteorological Society*, *79*(11), 2457–2476. https://doi.org/10.1175/1520-0477(1998)

Rosenfeld, D., & Woodley, W. (2001). Pollution and clouds. *Physics World*, *14*(2), 33–37.

Rosenfeld, D., Lohmann, U., Raga, G. B., O'Dowd, C. D., Kulmala, M., Fuzzi, S., … Andreae, M. O. (2008). Flood or drought: How do aerosols affect precipitation? *Science*, *321*, 1309–1313. https://doi.org/10.1126/science.1160606

Sekiguchi, M., Nakajima, T., Suzuki, K., Kawamoto, K., Higurashi, A., Rosenfeld, D., … Mukai, S. (2003). A study of the direct and indirect effects of aerosols using global satellite data sets of aerosol and cloud parameters. *Journal of Geophysical Research*, *108*(D22), 4699. https://doi.org/10.1029/2002JD003359

Shao, H. F., & Liu, G. S. (2005). Why is the satellite observed aerosol's indirect effect so variable? *Geophysical Research Letters*, *32*, L15802. https://doi.org/10.1029/2005GL023260

Stevens, B., & Feingold, G. (2009). Untangling aerosol effects on clouds and precipitation in a buffered system. *Nature*, *461*(7264), 607–613. https://doi.org/10.1038/nature08281

Stowe, L. L., Ignatov, A. M., & Singh, R. R. (1997). Development, validation, and potential enhancements to the second-generation operational aerosol product at the national environmental satellite, data, and information service of the national oceanic and atmospheric administration. *Journal of Geophysical Research*, *102*(D14), 16,923–16,934.

Twomey, S. (1974). Pollution and planetary albedo. *Atmospheric Environment*, *8*(12), 1251–1256. https://doi.org/10.1016/0004-6981(74)90004-3

Twomey, S. A. (1977). Pollution and cloud albedo. *Transactions - American Geophysical Union*, *58*(8), 797–797.

Twomey, S., & Squires, P. (1959). The influence of cloud nucleus population on the microstructure and stability of convective clouds. *Tellus*, *11*(4), 408–411. https://doi.org/10.1111/j.2153-3490.1959.tb00050.x

Twomey, S. A., Piepgrass, M., & Wolfe, T. L. (1984). An assessment of the impact of pollution on global cloud albedo. *Tellus Series B: Chemical and Physical Meteorology*, *36*(5), 356–366.

Walther, A., & Heidinger, A. K. (2012). Implementation of the Daytime Cloud Optical and Microphysical Properties algorithm (DCOMP) in PATMOS-x. *Journal of Applied Meteorology and Climatology*, *51*, 1371–1390. https://doi.org/10.1175/Jamc-D-11-0108.1

Yuan, T. L., Li, Z. Q., Zhang, R. Y., & Fan, J. W. (2008). Increase of cloud droplet size with aerosol optical depth: An observation and modeling study. *Journal of Geophysical Research*, *113*, D04201. https://doi.org/10.1029/2007JD008632

Zhao, X.-P., Dubovik, O., Smirnov, A., Holben, B. N., Sapper, J., Pietras, C., … Frouin, R. (2004). Regional evaluation of an advanced very high resolution radiometer (AVHRR) two-channel aerosol retrieval algorithm. *Journal of Geophysical Research*, *109*, D02204. https://doi.org/10.1029/2003JD003817

Zhao, X. P., Heidinger, A. K., & Walther, A. (2016). Climatology analysis of aerosol effect on marine water cloud from long-term satellite climate data records. *Remote Sensing*, *8*(4), 300. https://doi.org/10.3390/Rs8040300